Renewable Energy 177 (2021) 1087–1101

Contents lists available at ScienceDirect

Renewable Energy

journal homepage: www.elsevier.com/locate/renene

Economic and thermo-mechanical design of tubular sCO_2 central-receivers

M. Fernández-Torrijos *, P.A. González-Gómez , C. Sobrino , D. Santana

Universidad Carlos III de Madrid, ISE Research Group, Thermal and Fluid Engineering Department, Avda. de la Universidad 30, 28911, Leganés, Madrid, Spain

ARTICLE INFO

Article history:
Received 23 February 2021
Received in revised form
5 May 2021
Accepted 9 June 2021
Available online 13 June 2021

Keywords:
Solar receiver
Creep-fatigue damage
Heliostat field
Thermal stress
sCO_2

ABSTRACT

Supercritical CO_2 central-receivers must withstand high temperatures and pressures combined with cyclic operation, which makes the solar receiver susceptible to creep-fatigue failure. In this work, a creep-fatigue analysis of a sCO_2 Inconel 740H tubular receiver of a 2 MW_e solar tower plant has been accomplished to study the influence of the tube size on the receiver and solar field design. A 2D numerical model of the tubular receiver that accounts for the thermal conduction in both radial and circumferential directions was developed to determine the sCO_2 and wall temperature profile, which is crucial for the creep-fatigue calculations. The receiver flux distribution, which is an input to the model, was obtained with SolarPILOT, while a conventional recompression model was used to calculate the cycle efficiency and inlet temperature to the receiver. Comparison of the results of the 2D model with those of a 1D model showed that the 1D model overestimates the creep fatigue rupture time by two orders of magnitude. Furthermore, the efficiency and costs of the heliostat field and receiver were calculated for different receiver tube sizes. Smaller tubes allowed a higher maximum heat flux leading to smaller receiver and heliostat field designs, which resulted in higher overall efficiency of the power plant and lower material costs. For a design ensuring 25 year receiver lifetime the minimum sCO_2 solar receiver cost, 345 €/kW_{th}, was obtained for the smallest pipe diameter.

1. Introduction

CSP with up to 1.5 GWh of thermal energy storage (TES) increases the flexibility of the electricity system, avoiding the need for fossil fuel back up and making it easier to integrate renewable energy sources with a variable output, such as photovoltaics (PV) and wind energy.

Several Key Performance Indicators (KPI) have been identified to evaluate the success in the implementation of CSP technology [1]. The overarching KPI is the supply price for dispatchable electricity (without the need for fossil-fuel back-up). Today's most advanced CSP systems are central receivers (also called solar power towers) integrated with 2-tank TES, working with nitrate molten salt both in the receiver and in the storage system and delivering thermal energy at 565 °C for integration with conventional steam-Rankine power cycles. Increasing the heat transfer fluid (HTF) temperature and the efficiency of the power block by replacing actual subcritical steam cycles by supercritical CO_2 (sCO_2) cycles is one of the strategies proposed to reduce the cost of CSP electricity [2,3]. The receiver of such a configuration would be working under high temperatures (≤700 °C) and high heat flux (0.3–1 MW/m^2). Direct heating of the sCO_2 in the receiver has been considered as an option that would overcome the problem of maximum operating temperature and freezing of the HTF associated to molten salt [4]. Challenges of direct type sCO_2 receiver is that they must withstand a high temperature and pressure, that reach 700 °C and 200 bar, which are usual temperature and pressure values at the turbine inlet. One of the main problems in using a gas such as CO_2 as the heat transfer fluid in a receiver is the lower internal heat transfer coefficients that are achieved. Moreover, the lower internal heat transfer coefficient of CO_2 in comparison to liquid HTF results in a higher temperature of the receiver tube surface [5]. Standalone on-sun tests were carried out successfully for a CO_2 cavity receiver working with subcritical CO_2 at a pressure of 700 kPa reaching CO_2 temperatures of 750 °C and tube temperature of 1050 °C [5]. A subcritical configuration was selected in this case because thermal storing system using CO_2 was pursued and the supercritical option was impractical at the moment due to material limitations relating to containment wall thickness required and corrosion of candidate

* Corresponding author.
E-mail address: ftorrijo@ing.uc3m.es (M. Fernández-Torrijos).

https://doi.org/10.1016/j.renene.2021.06.047
0960-1481/

metals. The combination of elevated temperature operation and cyclic behavior makes solar receiver susceptible to creep-fatigue failure. This risk is even more critical at the higher temperatures of sCO_2 receivers compared to commercial molten salt plants. Code Case N-47 [6] and Section III-NH of ASME Boiler and Pressure Vessel Code [7] have been applied in the past for the creep-fatigue evaluation of solar receivers. Because those standards were written for nuclear components the criteria become too conservative for solar receivers resulting in excessive economic penalties [8]. Nithyanandam et al. [9] conducted a thermo-mechanical simulations of a sCO_2 receiver tube concluding that the optimum design for highest thermal efficiency requires tubes of smaller radius and higher heat flux at the expense of higher pressure drop, however the results presented were for an axisymmetric temperature distribution in the receiver tubes which largely reduces the stress level compared to the non-axisymmetric temperature distribution obtained with conventional central receiver configurations. Besides, plastic deformation or stress relaxation were not considered in the creep-fatigue analysis. Ortega et al. [10] used ANSYS software to calculate the thermal and mechanical stresses of a sCO_2 receiver tube with a non uniform temperature distribution characteristic of central receivers and perform a creep-fatigue analysis. For the case presented, only 86% of the nodes of the geometry surpassed the required lifetime. They suggested to reduce the flux and the wall thickness to decrease the thermal stresses. Nevertheless, again, the stress relaxation effect on the creep-fatigue assessment was not considered despite of its high impact on the lifetime estimation. Neises et al. [11] performed a preliminary creep-fatigue analysis of a simplified sCO_2 receiver tube, indicating that circumferential flux variation, not accounted in their analysis may significantly decrease the maximum allowable flux and should be included in further research.

According to the literature review, the main conclusion is that the available works focused on sCO_2 receivers did not consider the not negligible material effects such as plastic deformation and stress relaxation for the creep-fatigue analysis to accurately determine the lifetime on the receiver and the maximum allowable heat flux. According to Ref. [12], considering aforementioned material effects on the aiming strategy may lead to an improvement on the combined solar field-receiver efficiency by a factor of 2 compared to aiming strategies based on conventional stress limit methods. It should be noted that the maximum allowable heat flux sets the solar field and receiver sizes, which are one of the main investment costs of a solar power plant.

The present paper presents results of the temperature field and thermal and pressure stresses for a sCO_2 tubular receiver, varying the external diameter of the tubes. A two dimensional thermal model was applied considering conduction in radial and circumferential direction and the creep and fatigue damage interaction was evaluated. Finally the cost of the receiver panels and solar field for the different tube sizes were compared. The creep-fatigue analysis is based on the procedure proposed by Ref. [12] that calculates the stresses under elastic-plastic regime and the stress relaxation due to visco-elastic behavior of the material, using a low-computational cost method. The methodology is based on the ASME Section III-NH [7] but including some modifications to provide a sufficient level of safety and reliability for CSP applications but without imposing the excessive economic penalties.

2. Numerical modeling

2.1. External receiver characteristics

In solar tower power plants, the central receiver is located at the top of a tower, and it is formed by vertical thin-walled tubes connected in parallel to form a panel, through which the heat transfer fluid flows. The receiver consists of several panels connected in series or parallel, depending on the established flow pattern. Tubular receptor can be cavity-type, where the tubes are located inside an enclosure with an aperture to the heliostat field, or external type. The heliostats can be specially distributed in two main configurations depending of the type of the central receiver: north field for flat external or cavity receivers, and circular field for circular external receivers.

In this work, a flat external-type receiver with panels connected in series was chosen to study the influence of the receiver tube diameter size on both field and receiver designs for solar tower power plants working with a supercritical CO_2 cycle, with a turbine operating at an inlet pressure of 20 MPa and an inlet temperature of 700 $^{\circ}C$. The sCO_2 flat external receiver used in this work consists of parallel straight tubes of height $H_t = 9.6$ m, that gather into panels, through which the sCO_2 flows. Each panel includes an inlet and an outlet header, inlet and outlet nozzles, and several tubes (see Fig. 1). The sCO_2 enters in the receiver through the eastern panel at low temperature, passes through the panels of the receiver, as a serpentine, and leaves the receiver through the western panel at 700 °C. In each panel the sCO_2 flow is divided into the tubes (N_t) that make part of the panel. The distance between the receiver tubes (B) is fixed to 2 mm. The material of the tubes is Nickel-based alloy Inconel 740H.

The purpose of this work is to study the thermo-mechanical behavior of the receiver to evaluate its reliability under creep and fatigue conditions. Besides, the capital and manufacturing costs of both receiver and heliostat field were calculated for different receiver tube diameters to obtain the cost trend with the tube size. Thus, three cases with different tube external radius were considered: i) Case 1: $r_o = 6.2$ mm, ii) Case 2: $r_o = 12.4$ mm and iii) Case 3: $r_o = 21$ mm.

As a design condition, the sCO_2 velocity through both the receiver tubes and headers is set to the maximum allowed to avoid noise or vibration problems [13].

$$u_{max} = \frac{175}{(\rho_f(700^{\circ}C))^{0.43}} \tag{1}$$

The sCO_2 mass flow rate to provide a net power output of 2 MW_e in the cycle and to have a solar multiple of approximately 2.3 ($SM = \dot{Q}_{th,sf}/\dot{Q}_{th,pb}$) is

$$\dot{m} = \frac{\dot{W}_{PB}\, SM}{(h_{f,out} - h_{f,in})\, \eta_{PB}} \tag{2}$$

where η_{PB} is the efficiency of the recompression cycle used in this work (see Section 2.3), $h_{f,in}$ is the sCO_2 receiver inlet specific enthalpy, which is slightly different for each receiver tubes size considered (see Section 2.3), and $h_{f,out}$ is the sCO_2 receiver outlet specific enthalpy.

The number of tubes per panel for the three different cases was calculated as

$$N_t = \frac{\dot{m}}{\rho_f(700^{\circ}C)\, u_{max}\, A_s} \tag{3}$$

where A_s is the cross-sectional area of a tube.

The tubes and headers thickness for each tubes external diameter considered was selected according to Ref. [14] for pressurized tubes and pipes:

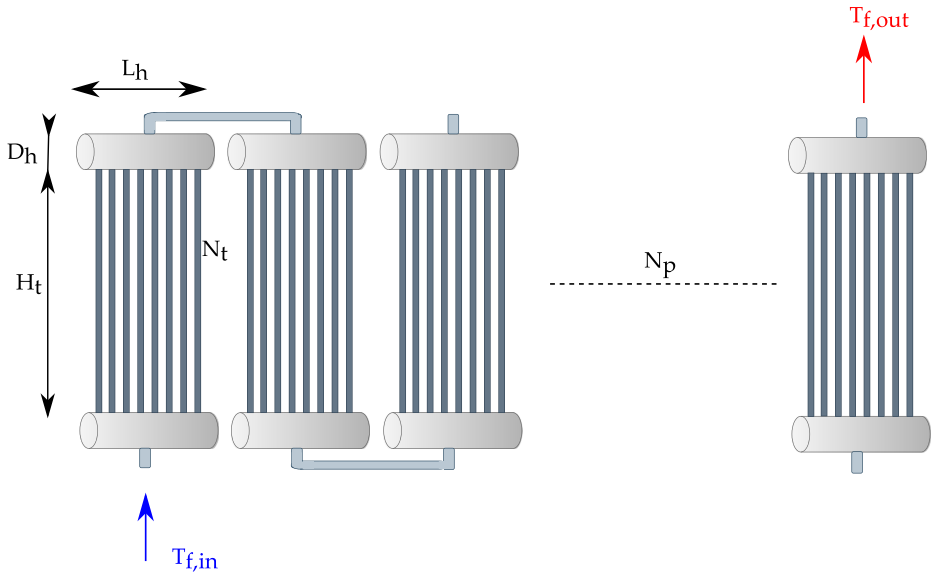

Fig. 1. Schematic of the receiver.

$$t = \frac{P r_o}{SE + 0.4P} = \frac{P r_i}{SE - 0.6P} \tag{4}$$

where P is the internal pressure in the receiver (20 MPa in this case), S is the maximum allowable stress value (34.5 MPa for the maximum temperature allowed of 800 °C [15]), r_o is the external radius, r_i is the internal radius, and E is the joint efficiency factor. For seamless tubes E = 1. When the thickness exceeds one-half of the inside radius

$$t = r_o\left(1 - \exp\left[\frac{-P}{SE}\right]\right) = r_i\left(\exp\left[\frac{P}{SE}\right] - 1\right) \tag{5}$$

where the tube and headers thicknesses obtained for the three different cases are shown in Section 3.

Solar tower receiver tubes are subjected to a high non uniform heat flux that results in high temperature differences between the front and rear sides of the tubes, which causes thermal stress and tube bending. As the tubes in the panels are separated between them only 2 mm, thus to avoid overheating of the tubes by contact, each tube is periodically guided over its entire length by clips welded to the tube surface to restrain the tubes from bowing outwards and laterally. In this work, clips are located every 2 m along the receiver tubes [16]. The total number of clips obtained for the three different receiver diameters studied is shown in Section 3.

2.2. Solar field and incident flux on the receiver

In this work, the heliostat field design was obtained from SolarPILOT, an open source software that creates heliostat field layouts that account for local solar and atmospheric conditions, receiver geometry and tower height, and simulate receiver flux profiles using both the analytical Hermite polynomial expansion flux mapping technique and Monte Carlo ray-tracing engine with SolTrace [17]. The solar power plant simulated in this work is located in Albuquerque. The desing-point DNI of the solar power plant was set to 950 W/m^2 on summer solstice. The solar field design power was approximately 10 MW_t, as the solar multiple was 2.3, the sCO_2 cycle was designed to provide 2 MW_e, and the cycle efficiency was around 47% (see Table 2). The tower height was set to 100 m, the solar field layout method was established as radial stagger with no blocking-dense. The heliostat field is formed by N_h heliostats of 12.2 × 12.2 m^2, which concentrates the radiation onto the flat receiver. The aperture of the receiver (A_R) is calculated as the minimum area that fulfill two conditions: i) the outlet temperature of the receiver must be 700 °C; ii) the lifetime of the receiver must be 25 years. To ensure that these conditions are fulfilled, a finite-volume numerical model of a sCO_2 flat tubular receiver was developed to obtain both sCO_2 and wall temperature profiles from the receiver flux distribution obtained with SolarPILOT. A trial-error methodology was conducted: first, the solar field was simulated with SolarPILOT, then, the incident heat flux on the receiver was established as an input of the finite-volume model to calculate both the sCO_2 outlet temperature and the wall temperature profile, which is crucial to calculate the receiver lifetime by means of the creep-fatigue analysis. If the sCO_2 outlet temperature is not 700 °C, or the receiver lifetime is not 25 years, the solar field is redesigned with SolarPILOT, and the new incident heat flux is considered as the input of the finite-volume model. The large number of tubes in the receivers makes a detailed simulation computationally expensive. To reduce the computational cost of the numerical model simulations, a representative tube that receives the mean heat flux at each axial position of each panel of the receiver was selected to calculate the sCO_2 outlet temperature. Rodríguez-Sánchez et al. [18] studied the influence of simulating one representative tube per panel instead of the whole receiver on the yield production of the power plant results, and obtained an error below 2.5%. However, to accurately estimate the temperature profile and the thermal stress of the tubes to calculate the receiver lifetime, a more detailed simulation is needed [18]. As the more critical point of the receiver in terms of lifetime is usually the tube section that receives the maximum heat flux, a representative tube that receives the maximum heat flux of each panel of the receiver was selected for obtaining the wall temperature profiles that are used to determine the receiver lifetime.

2.3. Supercritical carbon dioxide power cycle

A conventional recompression cycle (Fig. 2) is modeled to calculate the cycle efficiency and the temperature at the receiver inlet. The CSP plant working with sCO_2 as the HTF in the receiver and operating with a sCO_2 cycle would need a thermal storage system to be able to operate at any time day or night. Carbonate

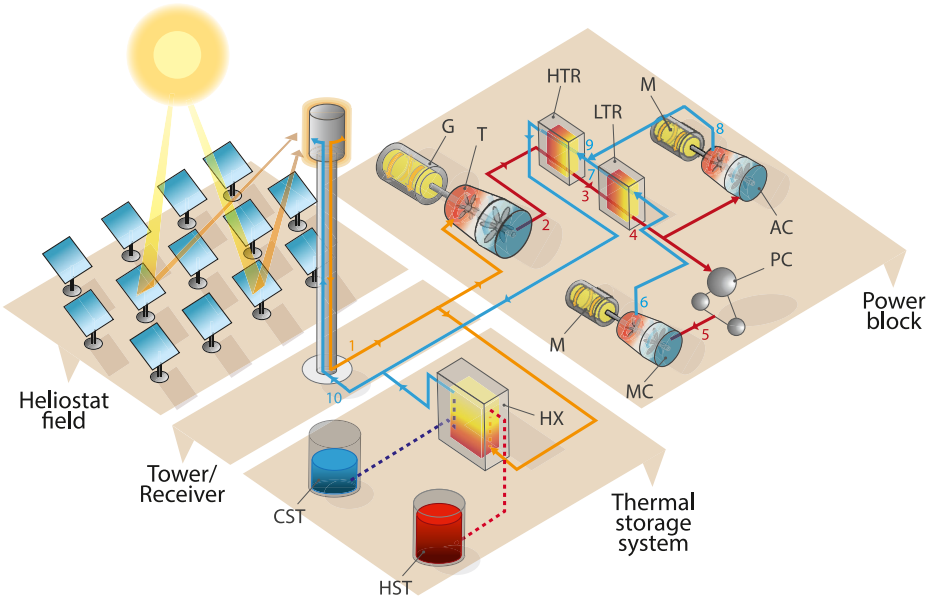

Fig. 2. Schematic of the CSP plant with a sCO_2 recompression cycle.

molten salt (Li_2CO_3–Na_2CO_3–K_2CO_3), with a melting point slightly under 400 °C and good stability up to 700 °C, has been demonstrated to be a suitable candidate for a two tank sensible heat storage system at high temperatures [19]. Since the thermal power delivered by the solar field is higher that the thermal power needed by the power cycle to work under nominal conditions ($SM > 1$), part of the sCO_2 coming from the receiver is sent to the sCO_2 - molten salt heat exchanger (Fig. 2) during the charging cycle of the thermal storage system to transfer thermal energy from the sCO_2 to the molten salt on its way from the cold to the hot tank.The equations applied to each component of the cycle are summarized in Table 1. The pressure at the turbine inlet is set to 200 bar and its temperature to 700 °C. The pressure at the main compressor inlet is set to 79 bar and its temperature to 32 °C, corresponding to a wet cooling scenario. Configuration (axial or radial) of the turbomachinery mainly depends on the cycle power level. Generally, radial-flow turbomachinery is preferred for small-scale cycles with power level less than 10 MW, while an axial-flow turbomachinery is adopted for higher power level cycle systems [20]. Besides, conventional sealing technology in sCO_2 cycle turbomachinery can result in an efficiency penalty as high as 0.55–0.65% due to the inherent characteristics of sCO_2 and the high rotational speeds. However new barrier gas methods are being investigated to reduce the penalty in the turbine power due to the increased leakage flow rate to only 0.15%, which is insignificant compared to the power saving in the leakage compression power [21]. Therefore, isentropic efficiencies of 83.37%, 81% and 81.76% are taken for the turbine, main compressor and auxiliary compressor respectively [20]. The pressure drops for precooler (PC), low temperature recuperator (LTR) and high temperature recuperator (HTR) are set to 0.4 bar [22] and approach temperatures of 6 °C and 16 °C were considered for the LTR and HTR respectively, in accordance with the ranges established in Ref. [23]. The ratio of cold to hot mass flow rate streams at LTR, α, is that needed to have the same temperature approach at both extremes of the LTR. The receiver pressure drop is calculated using Equation (14). The state points of the cycle for three different receiver designs with different values of the outer radius of the tubes, can be found in Table 2 and are represented in the T-s diagram of Fig. 3 for the case of receiver tubes with an external radius of $r_o = 6.2$ mm.

Table 1
sCO_2 cycle modeling.

MC	$\dot{W}_{MC} = \alpha\,\dot{m}\,(h_6 - h_5)$
	$\eta_{PB} = \dfrac{h_{6s} - h_5}{h_6 - h_5}$
AC	$\dot{W}_{MC} = (1-\alpha)\,\dot{m}\,(h_8 - h_4)$
	$\eta_{PB} = \dfrac{h_{8s} - h_4}{h_8 - h_4}$
T	$\dot{W}_T = \dot{m}\,(h_1 - h_2)$
	$\eta_T = \dfrac{h_1 - h_2}{h_1 - h_{2s}}$
Receiver	$\dot{Q}_R = \dot{m}\,(h_1 - h_{10})$
	$\Delta P = P_{10} - P_1$
HTR	$\dot{Q}_{HTR} = \dot{m}\,(h_2 - h_3)$
	$(h_2 - h_3) = (h_{10} - h_9)$
	$\Delta P_{CO2} = P_2 - P_3$
	$\Delta P_{CO2} = P_9 - P_{10}$
	$PP_{HTR} = T_3 - T_9$
LTR	$\dot{Q}_{LTR} = \dot{m}\,(h_3 - h_4)$
	$(h_3 - h_4) = \alpha\,(h_7 - h_6)$
	$\Delta P_{CO2} = P_3 - P_4$
	$\Delta P_{CO2} = P_6 - P_7$
	$PP_{LTR} = T_3 - T_7$
	$PP_{LTR} = T_4 - T_6$
PC	$\dot{Q}_{PC} = \dot{m}\,\alpha\,(h_4 - h_5)$
Junction	$P_8 = P_9 = P_7$
	$\alpha\,h_7 + (1-\alpha)\,h_8 = h_9$

2.4. Thermal model

The numerical model developed in this work solves the steady state heat transfer problem of a tubular external sCO_2 receiver. The temperature of the tubes is assumed to vary in axial, radial and circumferential directions of each tube. For simplicity, only one tube per panel has been studied, considering that every tube in a panel receives the same radiation flux [18].

The mass and energy balance of sCO_2 is fulfilled by Equations (6) and (7)

$$\frac{\partial}{\partial t}(\rho_f(z)) + \frac{\partial}{\partial z}(\rho_f(z)\,u(z)) = 0 \tag{6}$$

Table 2
State points and cycle efficiency of the sCO_2 recompression cycle for the three different receiver designs.

	$r_o = 6.2$ mm			$r_o = 12.4$ mm			$r_o = 21$ mm		
	P (bar)	T (°C)	h (kJ/kg)	P (bar)	T(°C)	h (kJ/kg)	P (bar)	T (°C)	h (kJ/kg)
1	200	700	1223.3	200	700	1223.3	200	700	1233.3
2	80.2	587.3	1089.8	80.2	587.3	1089.8	80.2	587.3	1089.8
3	79.8	186.8	624.7	79.8	188.6	626.7	79.8	192.4	631.1
4	79.4	65.2	468.5	79.4	65.6	469.2	79.4	66.4	470.6
5	79	32	298.8	79	32	298.8	79	32	298.8
6	206.1	59.2	321.1	208.4	59.6	321.5	213.4	60.4	322.3
7	205.7	180.8	568.6	208	182.6	570.4	213	186.4	574.2
8	205.7	154.5	528.1	208	156.2	529.8	213	159.6	533.4
9	205.7	170.8	553.6	208	172.6	555.5	213	176.4	559.4
10	205.3	537.1	1018.7	207.6	537	1018.5	212.6	537	1018.1
η_{PB}(%)		47.6			47.3			46.6	

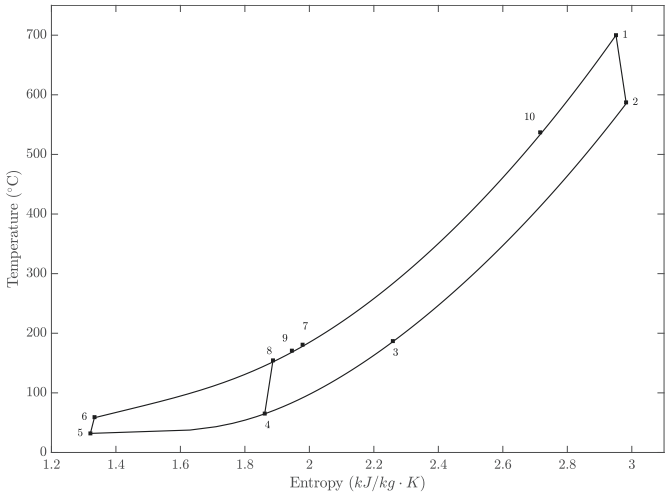

Fig. 3. T-s diagram of the power cycle.

$$\rho_f(z)\, c_{p,f}(z)\, \frac{\partial T_f(z)}{\partial t} + \rho_f(z)\, u(z)\, c_{p,f}(z)\, \frac{\partial T_f(z)}{\partial z} = h_i(z)\, a_w \Big(T_w(z) - T_f(z) \Big) \tag{7}$$

where T_f is the sCO_2 bulk temperature, ρ_f, $c_{p,f}$ are the sCO_2 density and specific heat, respectively, which depends on the sCO_2 temperature and have been obtained using Cool Prop library. u is the sCO_2 velocity, $a_w = 4/d_i$ is the inner wall surface area per unit of volume, and $\bar{T}_w$ is the mean inner surface temperature for each axial position. h_i is the internal convective coefficient which has been calculated using Petukhov's correlation for gases [24] Caliot and Flamant [25] showed that for a turbulent flow, radiation has negligible influence on the heat transfer of sCO_2; thus, only convective heat transfer method is considered at the inner surface. Heat transfer deterioration must be considered for sCO_2 applications where the operating temperatures and pressures are close to sCO_2 pseudocritical line, where fluid properties such as density and enthalpy show property changes intermediate to those of liquid and gas, with large gradients from liquid-like to gas-like. The gradients get lower when the pressure and temperature are away from the critical point [26,27]. Although the precise mechanism of a heat transfer deterioration is not well understood, Kurganov and Kaptil'nyi [28] experimentally verified that an M-shape velocity distribution and a distortion of the shear stress are the major causes of a heat transfer deterioration. Bae and Kim [29] proposed an experimental correlation to obtain the correction factor that accounts for the heat transfer deterioration, as a function of $Bu = \frac{\bar{Gr}}{Re^{2.7}\, Pr}$. They concluded that when Bu is small enough (i.e. $Bu < 10^{-8}$) the heat transfer can be predicted by typical correlations available in literature (i.e. Dittus-Boelter). When $10^{-8} < Bu < 10^{-4}$, the heat transfer decreases due to the M-shape velocity distribution caused by the existence of the point of the pseudo-critical temperature near the wall. When Bu becomes very large (i.e. $Bu > 10^{-4}$), the flow recovers from a deterioration and the heat transfer coefficient begins to increase, presumably due to the evolution of the velocity distribution from an M-shape to a normal velocity distribution in a turbulent flow. In this work, the parameter Bu in the solar receiver is around 10^{-10}, which means that heat transfer deterioration does not occurs in the receiver proposed in this work, as the operating pressure and temperatures are far from the critical point. Thus, sCO_2 is equivalent to a perfect gas for the receiver simulation purposes, in the working receiver conditions 200–213 bar and 537–700 °C, because the compressibility factor ranges from 0.96 to 1.002 in such working conditions [30].

The energy balance of the tube wall is fulfilled by Equation (8)

$$\rho_w\, c_{p,w} \frac{\partial T_w(r,\theta,z)}{\partial t} = \nabla \cdot (k_w(r,\theta,z)\, \nabla T_w(r,\theta,z)) \tag{8}$$

where ρ_w and $c_{p,w}$ corresponds to the Inconel 740H density and specific heat, which have been considered constant and equal to 8050 kg/m^3 and 542 J/kgK, respectively; k_w corresponds to the Inconel 740H thermal conductivity coefficient that depends on the wall temperature of the tube according to [15].

The outer wall thermal boundary condition is set to a mixed convective and radiative heat transfer condition. Thus, the boundary conditions of the problem are expressed as follows:

$$-k_w(r,\theta,z) \frac{\partial T_w(r,\theta,z)}{\partial r} = h_i(z)(T_f(z) - T_w(r,\theta,z)), \quad \text{at } r = r_i \tag{9}$$

$$-k_w(r,\theta,z) \frac{\partial T_w(r,\theta,z)}{\partial r} = \bar{h}_{nc}(T_w(z,\theta) - T_{amb}) + q(\theta,z), \quad \text{at } r = r_o \tag{10}$$

$$\frac{\partial T_w(r,\theta,z)}{\partial \theta} = 0, \quad \text{at } \theta = 0,\, \pi \tag{11}$$

$$\frac{\partial T_w(r,\theta,z)}{\partial z} = 0\,, \quad \text{at } z = 0,\, H_t \tag{12}$$

where h_{nc} is the natural convective heat transfer coefficient calculated as [31], since the wind velocity around the receiver is neglected, and q is the heat emit-ted by the tubes only con-sid-er-ing heat loss to the sur-round-ings due to ra-di-a-tion.

To take into account the radiative heat transfer on the receiver, the net radiation method was used [32]. The element of study is formed by two semi-tubes sited face to face, a rear surface thermally isolated that can be considered as a refractory wall, and an imaginary front surface totally transparent to solar irradiation and through which the energy reflected to the sky is lost (see Fig. 5). An artificial and punctual energy source representing an emitter of the reflected radiation is coming from the heliostat field (q_h), which has been obtained from the heliostat field design conducted with SolarPILOT (see Section 2.2).

$$\left[\frac{\delta_{m,0}}{\epsilon_0} - \left(\frac{1}{\epsilon_0} - 1\right) F_{m,0}\right] \frac{q_0}{\sigma_s} + \sum_{i=1}^{N_s} \left(\frac{\delta_{m,i}}{\epsilon_i} - \left(\frac{1}{\epsilon_i} - 1\right) F_{m,i}\right) \frac{q_i}{\sigma_s} -$$

$$\left[\delta_{m,N_s+1} - F_{m,N_s+1}\right] T_{N_s+1}^4 = \left[\delta_{m,0} - F_{m,0}\right] T_0^4 + \sum_{i=1}^{N_s} \left(\delta_{m,i} - F_{m,i}\right) T_i^4 -$$

$$\left[\frac{\delta_{m,N_s+1}}{\epsilon_{N_s+1}} - \left(\frac{1}{\epsilon_{N_s+1}} - 1\right) F_{m,N_s+1}\right] \frac{q_{N_s+1}}{\sigma_s} - F_{m,0} \frac{q_h}{\sigma_s} \alpha_s \tag{13}$$

where, the refractory wall and the imaginary surface, corresponding to the environment, are represented by the subscripts $N_s + 1$ and 0, respectively. T represents the effective temperature of radiation, T_0 is the surroundings temperature calculated according to Ref. [33], N_s is the number of surfaces in the circumferential direction, F is the view factor between surfaces calculated using the crossed-strings method [32], δ is the Kronecker delta, σ_s is the Stefan-Boltzmann constant, and α_s is the surface absortivity, which has been taken as 0.94, since the receiver tubes are coated with Black Pyromark, a paint of high absorptivity of the solar radiation. ϵ_0, ϵ_i and ϵ_{N_s+1} are the sky, tube wall and refractory wall emissivities, which have been taken as 0.895, 0.87 and 0.2, respectively. q is the heat emitted by the tubes only considering heat loss to the surroundings due to radiation. q_{N_s+1} represents the conductive losses through the refractory wall, which are null since the wall has been considered adiabatic.

The pressure drop along the receiver is calculated as

$$\Delta P = \sum_{i=1}^{N_p} \left(f_r \frac{H_t}{d_i} + K_{con} + K_{exp}\right) \frac{u^2(z)\,\rho_f(z)}{2} \tag{14}$$

where f_r is the friction factor for smooth tubes [24], $K_{con} = 0.45$ and $K_{exp} = 0.81$ are the contraction and expansion coefficients [34] considering that the inlet and outlet connections to the header are 2.54 cm in diameter [10].

2.4.1. Solution procedure

The governing equations were numerically solved using a finite volume method, with a second-order central differencing scheme for the derivative terms of temperatures and a first-order upwind scheme for the first derivative terms of velocity. Equations (6)–(8) were solved in Matlab by a time marching method to reach the steady state solutions of both sCO_2 and wall temperatures. The steady state is reached when the temperature difference between successive time steps is less than 0.001 K. The domain is divided into a uniform mesh in axial, radial and circumferential directions. The mesh size selected to carry out the simulations were $\Delta z = 19\ r_o$, $\Delta r = 0.5\ t_t$, $\Delta\theta = 10°$.

The temperature fields of the sCO_2 and the receiver wall were obtained using an explicit method; thus, in each time step n, the temperature fields were calculated from both temperature and velocity fields in the previous time step $n - 1$. After the temperature fields were solved in the current time step, the velocity field was obtained from Equation (15) that is derived from Equations (6) and (7)

$$\frac{\partial u}{\partial z} = \beta(z)\, \frac{h_i(z)\, a_w}{\rho_f(z)\, c_{p,f}(z)} \left(\bar{T_w}(z) - T_f(z)\right) \tag{15}$$

where $\beta = -\frac{1}{\rho_f} \frac{\partial \rho_f}{\partial T_f}$.

The criterion used for assessing code verification was the order of accuracy test, which determines whether or not the discretization error is reduced at the expected rate. The formal order of accuracy is determined by the truncation error, whereas the observed order of accuracy is the accuracy that is directly computed from code output for a given simulation [35]. The formal order of accuracy for sCO_2 and receiver wall temperatures is supposed to be a value between 1 and 2 as the derivative terms of temperature were solved using a second-order central differencing scheme, but the derivative terms of velocity was discretized using a first-order scheme. For calculating the observed order of accuracy when the exact solution is not known, three numerical solutions on different meshes are needed. The observed order of accuracy is calculated as follows [35].

$$p = \frac{\ln\left(\frac{\|f_3 - f_2\|}{\|f_2 - f_1\|}\right)}{\ln r_m} \tag{16}$$

where f_3 is the solution on the coarse mesh, f_2 the solution on the medium mesh, f_1 the solution on the fine mesh, and r_m is the grid refinement factor, which is the ratio between the coarse and the fine element sizes. In this work, a value of 1.75 was selected as grid refinement factor. Therefore, mesh sizes for the coarse mesh were $\Delta z_3 = 33\ r_o$, $\Delta r_3 = 0.875\ t_t$, $\Delta\theta_3 = 18°$; mesh sizes for the medium mesh, which is the mesh used for the calculations in this work, were $\Delta z_2 = 19\ r_o$, $\Delta r_2 = 0.5\ t_t$, $\Delta\theta_2 = 10°$; and mesh sizes for the fine mesh were $\Delta z_1 = 11\ r_o$, $\Delta r_1 = 0.29\ t_t$, $\Delta\theta_1 = 6°$. The order of accuracy of the wall temperature along the receiver height was approximately 1.5, which is in accordance with the formal order of accuracy, which indicates that the numerical code accurately solves the mathematical model incorporated. Solution verification consists in assessing the discretization errors present when partial differential equations are solved numerically. Grid Convergence Index (GCI) is a method for uniform reporting of grid refinement studies proposed by Roache [36]. The GCI provides an objective asymptotic approach to quantification of uncertainty of grid convergence, and is based upon a grid refinement error estimator derived from the theory of the generalized Richardson Extrapolation. The GCI is defined as follows

$$GCI = \frac{F_s}{r_m^p - 1} \left|\frac{f_2 - f_1}{f_1}\right| \tag{17}$$

where p is the order of accuracy, and F_s is a factor of safety that is usually set to three. The GCI obtained for wall temperature along the most critical section was 0.05%.

Besides, a simulation based on the Finite Element Method conducted with Abaqus software was carried out, and the maximum relative error committed for temperature calculations were 0.4%, whereas the error committed in the estimation of the maximum thermal stress along the tube section was 1%.

The radiation map obtained with SolarPILOT is a square grid of 25 × 25; thus, the radiation map grid needs to be interpolated to adapt it to the number of axial sections. To adapt the radiation map to the number of panels, a representative flux map has been selected for all the tubes of each panel (see Section 2.2).

2.5. Mechanical model

2.5.1. Thermo-elastic stress

The thermal stress on the receiver tubes is estimated according to the methodology described in Ref. [16]. Generalized plane strain (GPS) conditions have been considered to determine the stress on the receiver tubes. According to Ref. [16], GPS is a reasonable approach when the receiver tubes are supported by clips to prevent an excessive deformation. Note that GPS conditions allow the free axial expansion of the tubes resulting in zero axial section force and keeping constant the total strain in the axial direction.

Given the non-axisymmetric temperature profile on the tube walls, the thermo-elastic stress components ($\sigma^E_{T,i}$) are calculated considering the temperature dependence of the main mechanical properties, i.e., the Modulus of elasticity and the thermal expansion coefficient. Such approach is highly recommended due to the large temperature variations between the front and rear sides of the receiver tubes, where if the mechanical properties are considered temperature independent, the stress would be underestimated up to 20%. The values of the Modulus of elasticity and the thermal expansion coefficient for Alloy 740H are obtained from Ref. [37].

The high working pressure of sCO_2 receivers makes necessary the consideration of the pressure stresses for the structural integrity assessment. In this work, the pressure stress components for cylindrical coordinates ($\sigma^E_{P,i}$) are calculated according to Ref. [12]. Lastly, the thermal and pressure stresses are superimposed to obtain the total stress.

2.5.2. Stress-strain curve model

The time-independent strain is calculated as the sum of the elastic and plastic strains as:

$$\varepsilon = \varepsilon^E + \varepsilon^P \tag{18}$$

The elastic strain is calculated considering temperature dependent Elastic modulus as: $\varepsilon^E = \sigma/E$. The plastic strain of Alloy 740H is calculated using Ramberg-Osgood model for temperatures between 600 °C and 800 °C and Voce Hardening model for temperatures higher than 800 °C. These models are expressed in Equation (19) and the parameters are summarized in Table 3.

Table 3
Parameters of plastic strain models of Alloy 740H [2].

	σ_0 (MPa)	K (−)	n (−)	σ_p (MPa)	σ_1 (MPa)	δ (−)
600 °C–700 °C	400.24	0.0704	6.6480			
725 °C	374.20	0.0357	7.1315			
750 °C	348.16	0.0181	7.6150			
775 °C	312.255	0.0055	10.971			
800 °C	276.35	0.0017	14.327	574.991	455.850	908.324
825 °C				521.631	319.315	2212.205
850 °C				468.271	182.780	3516.087

$$\varepsilon_p = \begin{cases} 0 & \sigma \le \sigma_0 \\ K\left(\dfrac{\sigma-\sigma_0}{\sigma_0}\right)^n & \sigma > \sigma_0 \end{cases} \quad 600°C \le T \le 800°C$$

$$\varepsilon_p = \begin{cases} 0 & \sigma \le \sigma_1 \\ -\dfrac{1}{\delta}\ln\left(1-\dfrac{\sigma-\sigma_1}{\sigma_p-\sigma_1}\right) & \sigma > \sigma_1 \end{cases} \quad T > 800°C \tag{19}$$

2.5.3. Creep strain rate model

The creep strain rate must be considered to estimate the stress relaxation phenomenon which is essential to calculate properly the creep damage on the receiver [12]. The creep strain rate is calculated using the model proposed in Ref. [37] and based on theoretical formulations of [38,39] as:

$$\dot{\varepsilon}_c = \dot{\varepsilon}_0 \exp\left(\frac{B\,\mu\,b^3}{A\,k_B\,T}\right)\left(\frac{\sigma}{\mu}\right)^{\frac{-\mu\,b^3}{A\,k_B\,T}} \tag{20}$$

where $\dot{\varepsilon}_0$ is a reference strain rate, μ is the shear stress modulus ($\mu = E/(2(1+\nu))$), T is the absolute temperature, k_B is the Boltzmann constant and b is the characteristic Burgers vector. The rest of parameters of Equation (20) adjusted for Alloy 740H (A, B and $\dot{\varepsilon}_0$) are summarized in Table 4.

2.5.4. Creep damage

According to ASME Section III NH subsection [7] the creep damage should be evaluated using the Time Fraction rule as:

$$D_c = \int_0^{t_h} \frac{dt}{t_R(\sigma_{eff}, T)} \tag{21}$$

where the time to rupture is calculated using the following polynomial expression [40]:

$$\log(t_R) = -19.392 + \frac{23360}{T} + \frac{55321\log(\sigma_{eff})}{T} - \frac{2065\log(\sigma_{eff})^2}{T} - \frac{102.7\log(\sigma_{eff})^3}{T} \tag{22}$$

To estimate the time to rupture, it is first necessary to determine the effective creep stress, $\sigma_{eff} = (\sigma_{eq} - \sigma^{relax}_{eq})/K_{safe}$. The safety factor, K_{safe}, is considered equal to the unity due the following reasons: i) the equivalent stress is calculated using the von Mises criterion which largely underestimates the time to rupture due to creep damage under compressive stress state [41]; ii) the solar receiver failure is not especially dangerous and it would be reasonable consider a safety factor equal to the unity [42], reducing in this way the resulting economic penalties. The elastic-plastic

Table 4
Parameters of the creep strain model of Alloy 740H [2].

Parameter	Value	Units
$\dot{\varepsilon}_0$	$1.19 \cdot 10^{10}$	hr^{-1}
k_B	$1.38064 \cdot 10^{-20}$	mJ/K
b	$2.53 \cdot 10^{-7}$	mm
A	−10.98557	–
B	−0.53098	–

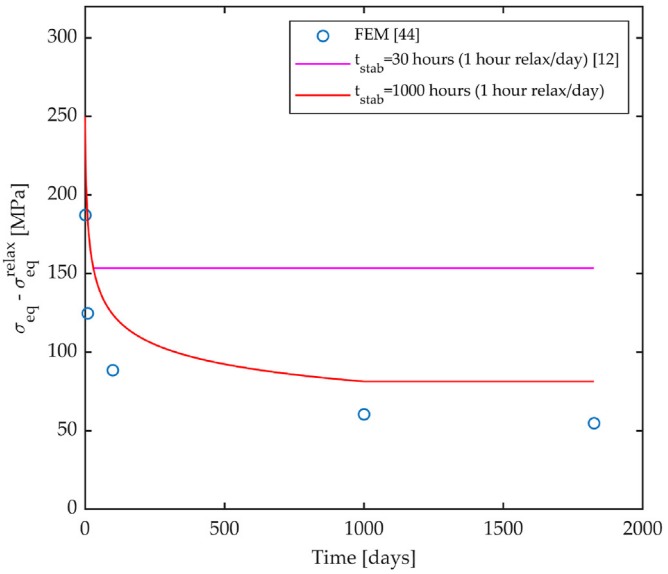

Fig. 4. Verification of the conservativeness on the stress relaxation calculation methodology proposed and compared against the FEM results of [44].

equivalent stress (σ_{eq}) is calculated considering three different cases:

1. The elastically calculated stress is lower than the yield strength, $\sigma^E_{eq} \leq S_y$: in this case, the material response is purely elastic and then the elastic-plastic equivalent stress is: $\sigma_{eq} = \sigma^E_{eq}$.
2. The elastically calculated stress (thermal and pressure) satisfies these two conditions: $\sigma^E_{T,eq} < 2\,S_y$ and $\sigma^E_{P,eq} + 1/\,4\sigma^E_{T,eq} < S_y$. At these conditions, cyclic elastic shakedown regime is obtained according to the Bree diagram [43]. The elastic-plastic equivalent stress can be estimated using the Neuber rule, when the elastic stress and strain are known: $\sigma^E_{eq}\,\varepsilon^E_{eq} = \sigma_{eq}\,\varepsilon_{eq}$
3. The elastically calculated stress does not satisfy the two aforementioned conditions and thus the material response is under cyclic plasticity or ratchetting conditions [43]. Due to the low lifetime expected, the heat flux on the receiver is reduced in order to avoid such working conditions.

Once the elastic-plastic stress is determined (σ_{eq}), the equivalent stress relaxation (σ^{relax}_{eq}) is calculated based on the methodology proposed by Ref. [12] and introducing additional modifications to consider the specific conditions of this study:

1. The stress relaxation stabilization time, t_{stab}, is fixed to 1000 h, considering only 1 h of relaxation per day during the first 1000 days of operation. To check the conservativeness of the proposed methodology, the stress relaxation calculated using the analytical method proposed in Ref. [12] is compared against FEM simulations results of a solar receiver of Alloy 740H [44], which has comparable working conditions of this work: generalized plane strain, 760 °C, 200 MPa. As can be seen in Fig. 4, $t_{stab} = 30$ h approach proposed originally in Ref. [12] may lead to a huge economic penalty due to the ultra-conservative stress relaxation estimation. However, $t_{stab} = 1000$ h yields a more reasonable approximation of the stress relaxation when it is comparted to FEM simulations and it still keeps a reasonable level of safety.
2. A stress relaxation limit should be considered due to the high working pressure of sCO_2 receivers. That limit is calculated in two steps: i) the normalized pressure stress ($X = \sigma^E_{P,eq}/S_y$) and the normalized thermal stress ($X = \sigma^E_{T,eq}/S_y$) are calculated; ii) these values are used to calculate the normalized lower bound stress $Z = \sigma_{LB}/S_{y,c}$ according Figure HBB-T-1332-1 of ASME Section III code [7], where the effective stress considering stress relaxation has to satisfy: $\sigma_{eff} \geq \sigma_{LB}$.

2.5.5. Fatigue

The fatigue damage of the receiver is estimated using the accumulated damage summation model following ASME Section III NH subsection [7] as:

$$D_f = \sum \frac{1}{N_{a,j}} \tag{23}$$

where the allowable number of cycles, $N_{a,j}$, of Alloy 740H is calculated as [37]:

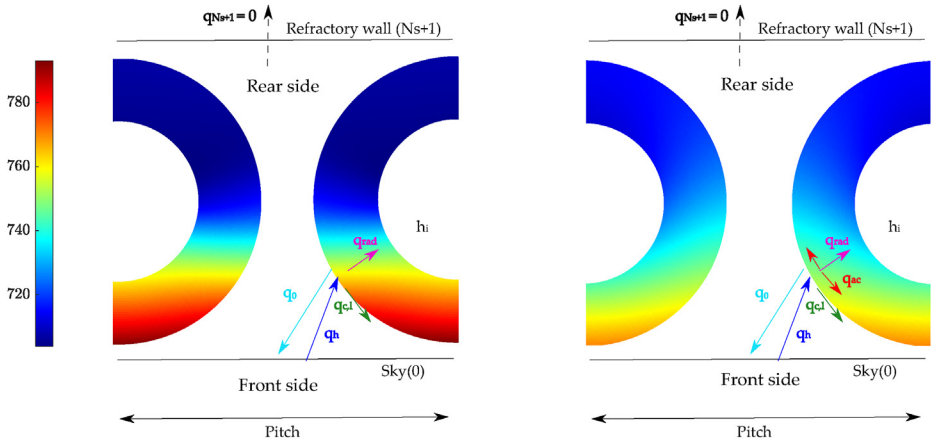

(a) 1D Model. (b) 2D Model.

Fig. 5. Geometry and coordinate system. Temperature profile in °C.

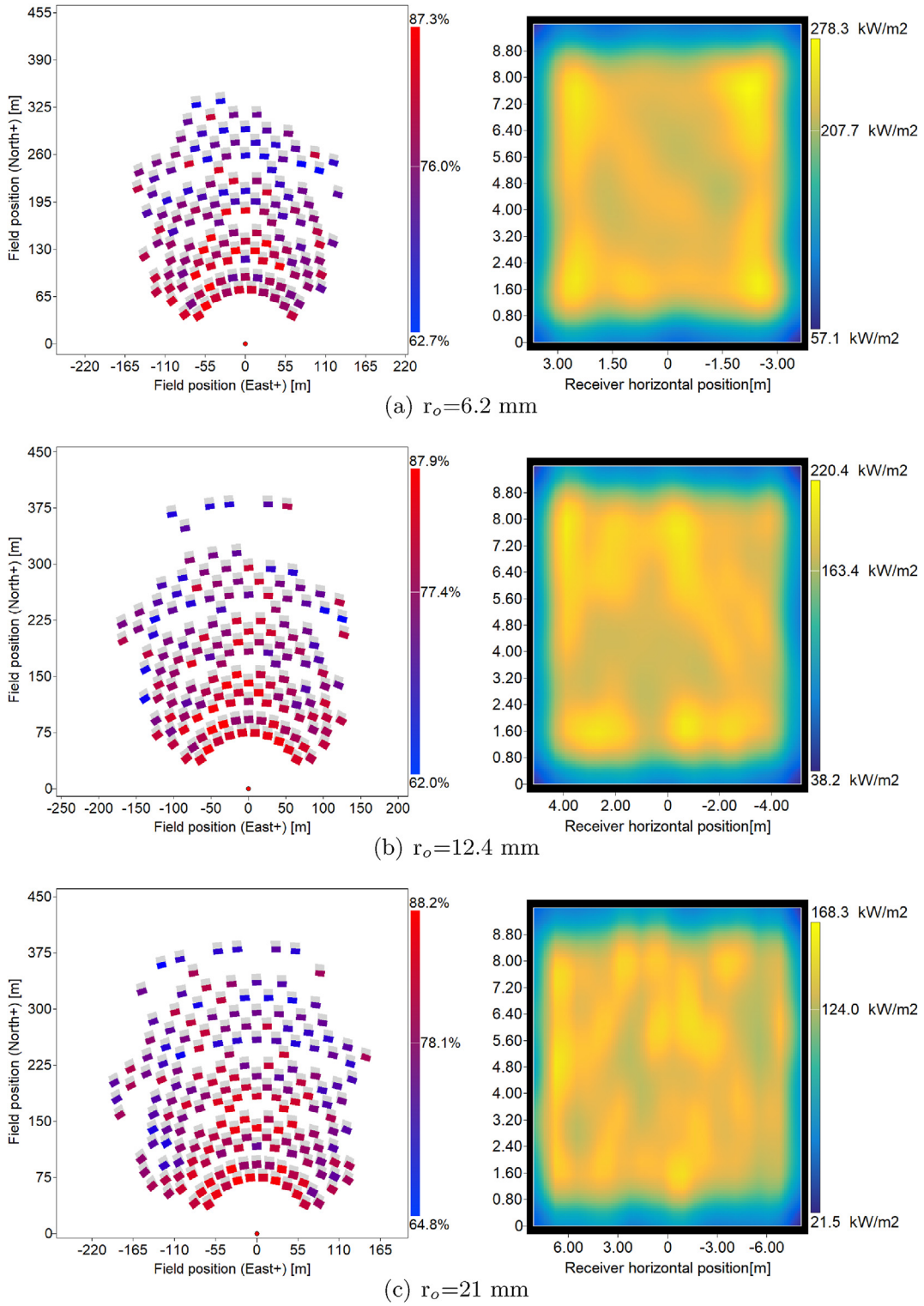

Fig. 6. Heliostats field (first column) and receiver incident heat flux (second column) for the three different designs considered varying the receiver external diameter.

$$\Delta\varepsilon_{eq} = \begin{cases} 0.0125 N_a^{-0.08} + 0.0765 N_a^{-0.44} & \text{if } T \leq 700°C \\ 0.0393 N_a^{-0.08} & \text{if } 700°C < T \leq 800°C \end{cases} \quad (24)$$

2.5.6. Creep-fatigue damage interaction

The combination of fatigue and creep damages may lead to a dramatical lifetime reduction of thermal devices, especially when both have a similar order of magnitude [45]. This phenomenon is captured by creep-fatigue interaction diagrams and their use allow the prediction of the lifetime when both mechanics of damage are combined. In the case of Alloy 740H, this diagram is not available in

Table 5
Receiver and heliostat field dimensions for the three different designs considered varying the receiver external diameter.

	$r_o = 6.2$ mm	$r_o = 12.4$ mm	$r_o = 21$ mm
Tube thickness, t_t (mm)	2.7	5.5	9.2
Tube height, H_t (m)	9.6	9.6	9.6
Number of tubes per panel, N_t (−)	508	128	46
Number of panels, N_p (−)	1	3	8
Receiver aperture A_R (m^2)	70.27	98.78	155.4
Header inner radius, $r_{i,h}$ (mm)	78.3	78.6	79.8
Header length, L_h (m)	7.32	3.43	2.02
Header thickness, t_h (mm)	61.5	61.7	62.7
Number of tube clips, N_c (−)	2438	1843	1766
Number of header's nozzles, N_n (−)	1016	768	736
Number of heliostats, N_h (−)	140	152	180
Heliostat field area A_{SF} (m^2)	20212	21945	25987

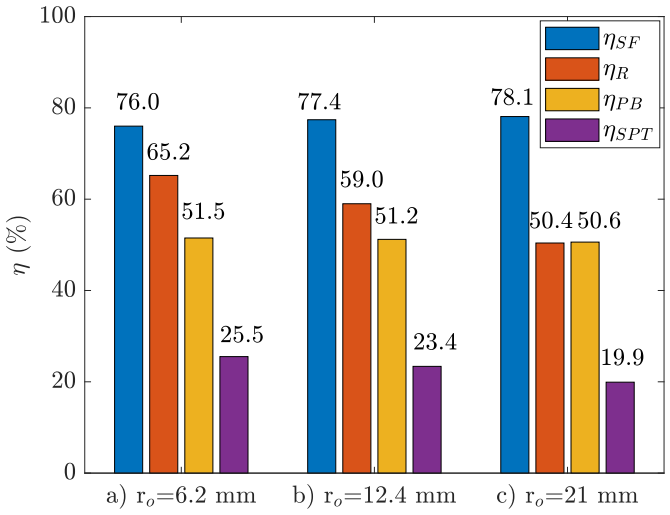

Fig. 7. Solar field optical efficiency, receiver efficiency, power block efficiency and overall efficiency.

the open literature. However, the diagram of nickel-based Alloy 617 can be assumed as a first approximation due to the similarities with Alloy 740H [46]. Therefore, the diagram to calculate the damage limit (D_L) is based on the bilinear rule with an intersection point of (0.1,0.1). Lastly, the lifetime on the receiver is estimated using the damage summation model as:

$$D_f + D_c = D_L \tag{25}$$

The creep and fatigue damages can be calculated for the design day as d_c and d_f. Then, the lifetime of the receiver can be estimated as equivalent operating days (EODs):

$$EODs \cdot d_f + EODs \cdot \dot{d}_c = D_L \rightarrow EODs = \frac{D_L}{d_f + \dot{d}_c} \tag{26}$$

Note that the daily creep damage, d_c, varies along the receiver lifetime due to the stress relaxation. In this work, it is considered a stabilization of the daily creep damage in 1000 days. Therefore, it is more convenient to be expressed as an average daily creep damage: $\dot{d}_c = D_c/EOD$.

3. Results

To accurately estimate the temperature profile along the tubes wall of the receiver, a complete two-dimensional model that considers thermal conduction in both radial an circumferential directions was developed in this work. The wall temperature profile obtained with the two-dimensional model was compared to these obtained with a simplified one-dimensional model that neglects thermal conduction in circumferential direction [47]. The Biot number $Bi = h_i\ t_t/k_w$ is the parameter that controls whether the local approach is valid: for high Biot numbers, the heat flux in circumferential direction is negligible compared to radial; for low Biot numbers, the opposite happens. Biot number in sCO_2 tubular receivers has an order of magnitude of 1; thus, thermal conduction in both radial and circumferential directions must be considered. Fig. 5 shows the comparison of the wall temperature profiles obtained with 1D and 2D models. As shown, 1D model overestimates in 22 °C the front-tube section temperature, resulting in higher temperature difference between the front and rear sides of the tube. The higher temperature of the front side of the tube results in lower creep and higher lifetime.

It should be noted that 1D thermal model has been extensively used to calculate the temperature on the receiver tubes [48,49]. However, a careful attention should be paid at low Biot numbers due to the large differences obtained in the temperature field between 1D and 2D thermal models [50]. The importance on the temperature field estimation is given by its huge impact on the stress estimation. In this specific case, a growth of 3% in the maximum temperature (from 771 °C to 793 °C) leads to an increase of 63% in the elastic stress (from 148.6 to 241.5 MPa). Such variation in the stress and temperature means a difference in the creep rupture time value of two orders of magnitude in the case of Alloy 740H [40].

Fig. 6 shows the comparison between the heliostat field and receiver designs for the three different tubes size considered. Smaller tubes results in higher maximum allowed heat flux onto the receiver to keep its lifetime above 25 years, which results in smaller receivers and heliostat fields. During the design process of both receiver and heliostat field with SolarPILOT, the mirrors aiming strategy was selected to obtain a uniform incident heat flux onto the receiver.

Table 5 shows the receiver and heliostat field dimensions obtained for the three different designs considered. As shown, the number of receiver panels increases with the tube diameter, but the number of tubes per panel decreases, so that the total number of receiver tubes decreases when the tube diameter increases.

Fig. 7 shows the solar field optical efficiency η_{SF}, receiver efficiency η_R, power block efficiency η_{PB} and overall efficiency $\eta_{SPT} = \eta_{SF} \cdot \eta_R \cdot \eta_{PB}$ for the three different designs considered varying the receiver external diameter. Since the receiver area and, therefore, the thermal losses are higher for bigger diameters, the receiver efficiency decreases when the receiver tubes size are increased. Although the solar field optical efficiency slightly increases with

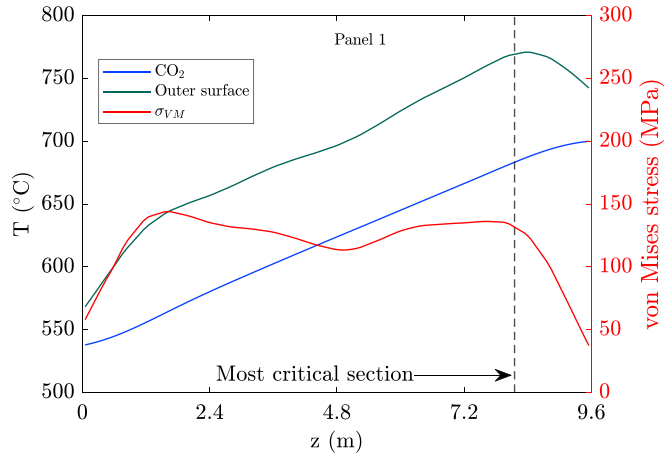

(a) r_o=6.2 mm

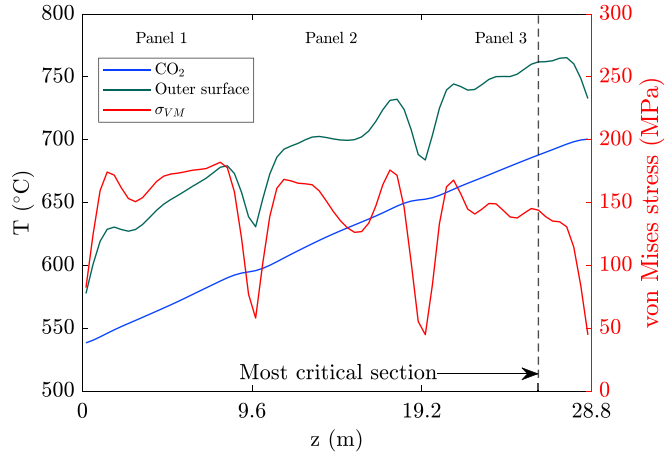

(b) r_o=12.4 mm

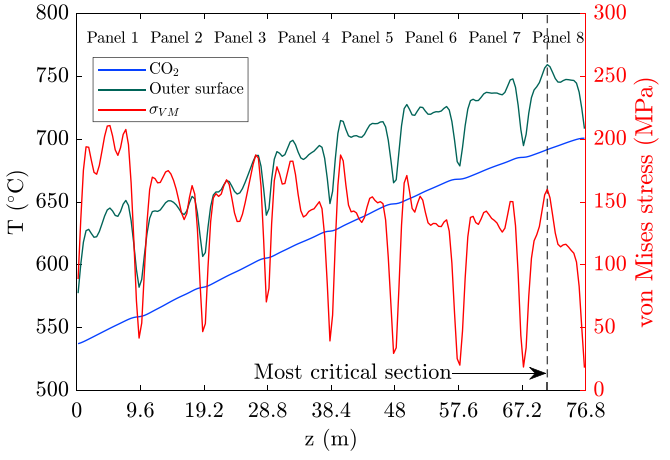

(c) r_o=21 mm

Fig. 8. Temperature (green line) and von Mises stress (red line) at the tube crown. sCO_2 bulk temperature (blue line).

tube diameter as the solar field is larger, the decrease of the receiver efficiency is more acute, so that the overall efficiency of the solar power plant is higher for smaller diameters.

Fig. 8 shows the temperature and von Mises stress profiles at the tube crown (outer surface at $\theta = 0$), and the sCO_2 bulk temperature. Besides, the most critical tube section in terms of lifetime is included: $z = 8.15$ m of panel 1 for $r_o = 6.2$ mm, $z = 6.6$ m of panel 3 for $r_o = 12.4$ mm, $z = 3.8$ m of panel 8 for $r_o = 21$ mm. Both sCO_2 and surface temperatures increases with the axial position for the three different receiver designs, reaching slightly higher maximum temperatures at the most critical section for smaller tubes. However, von Mises stress decreases with the axial position, as the temperature gradient in the tube walls is the highest in the first panel. The most critical tube section is located at the end of the last panel, where the wall temperature is maximum, although the thermal stress is lower than in the first panel. The most critical section is the point having the minimum lifetime of the receiver which has been set to 25 years. Since creep is the main mechanism of damage in the receiver, it makes sense that the critical points are obtained at the final panels which have the worst combination of high temperature and stress from the creep damage point of view. Note that the creep damage grows with the stress and temperature (see Equations (21) and (22)).

Fig. 9 shows the temperature and von Mises stress profiles along the most critical tube section for the three different receiver designs considered varying the external diameter. As explained before, smaller tubes result in higher maximum allowed heat flux, as the temperature differences along the cross section are lower for smaller tubes, which results in lower thermal stress that reduces creep and fatigue. As shown in Fig. 9 smaller tubes results in higher maximum allowed temperature.

3.1. Heliostat field and receiver costs

The capital cost of Inconel 740H was considered the same as Inconel 617 [51], which is 100 €/kg [52]. The receiver tubes were coated with Pyromark 2500, whose cost is 4.5 €/m^2 [53]. To obtain the manufacturing receiver cost, number of nozzles pulled from headers, tube-to-header welds, tube clip welds and tubes coating were considered. The man-hour rate was established at 53.5 €, whereas the labor hours per nozzles, tube-to-header welds, and tube clip welds, including leak detection, were 2, 1.5 and 1, respectively [54]. The coating application cost was considered as 240 €/m^2 [53]. The capital costs of heliostat field was considered as 120 €/m^2 [55]. The material and manufacturing costs of both receivers and heliostat field are shown in Table 6. The manufacturing costs of receiver increases when the tube diameter diminishes, as the number of tubes is higher for smaller tubes and, then, the number of nozzles pulled from headers and tube clips are higher (see Table 5). On the contrary, the material cost of tubes increases with the tube diameter due to the higher thickness required to withstand high pressures of 20 MPa. As shown in Table 5, lower tubes diameter results in smaller heliostat fields, as the allowed heat flux onto the receiver is higher for smaller tubes and, then, the receiver area is smaller. As heliostat field and receiver material costs dominate over receiver manufacturing costs, the total cost of both heliostats field and receiver decreases with a tube diameter reduction.

4. Conclusion

In this work, the influence of the receiver tube size on the thermo-mechanical behavior and lifetime of solar central receivers working with sCO_2 was studied. Thus, a 2-D model was developed to accurately determine the cross section temperature profiles

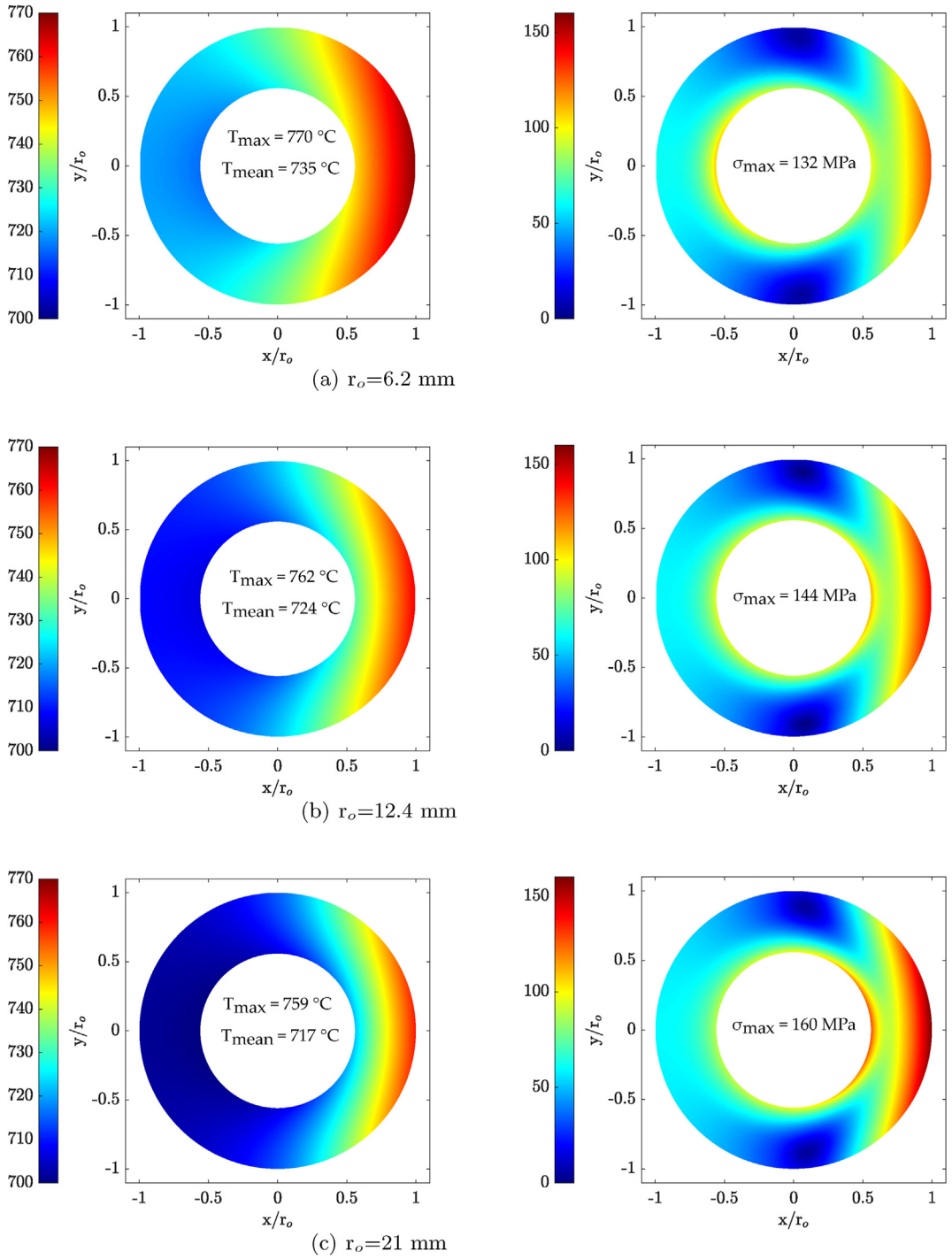

Fig. 9. Temperature profile in °C (first column) and von Mises stress profiles in MPa (second column) along the most critical tube section for the three different receiver designs (z = 8.15 m of panel 1 for r_o = 6.2 mm, z = 6.6 m of panel 3 for r_o = 12.4 mm, z = 3.8 m of panel 8 for r_o = 21 mm).

along the length of the receiver tubes, which is crucial to accurately calculate the creep-fatigue damage of the most critical section of the receiver to estimate its lifetime. The results of the 2D model were compared with those of a simplified 1-D model commonly used in molten salt receivers that neglects thermal conduction in circumferential direction. The design of both the heliostat field and the direct-heating sCO_2 tubular receiver was accomplished for different receiver tube sizes, to compare the influence of the tube diameter on both the efficiency and cost of the solar power plant. With this aim, the power plant was designed to deliver 2 MWe reaching sCO_2 temperatures of 700 °C at the outlet of the receiver, whose lifetime must be 25 years. The main conclusions of the study are:

1. 1D models are not appropriate for sCO_2 receivers, as the high working pressures around 20 MPa result in higher tube thickness, so that the heat flux in circumferential direction is not negligible compared to radial.

Table 6
Costs of heliostat field and receiver for the three different receiver designs considered varying the external diameter.

	$r_o = 6.2$ mm	$r_o = 12.4$ mm	$r_o = 21$ mm
Tubes material cost C_t (M €)	0.33	0.98	2.7
Coating material cost $C_{co,m}$ (M €)	0.0008	0.0004	0.0003
Coating application cost $C_{co,a}$ (M €)	0.046	0.023	0.014
Headers material cost C_h (M €)	0.25	0.35	0.57
Tube-to-header welds cost C_{we} (M €)	0.082	0.062	0.059
Nozzles cost C_n (M €)	0.11	0.082	0.079
Tube clip welds cost C_c (M €)	0.13	0.099	0.095
Total receiver cost C_R (M €)	0.94	1.60	3.52
Heliostat field cost C_{SF} (M €)	2.43	2.63	3.12
Total cost C_{SF+R} (M €)	3.37	4.23	6.64

2. Smaller tubes maximize the allowed heat flux onto the receiver which results in smaller receiver and heliostat field. This is due to a lower temperature difference along the cross section which results in lower thermal stress that reduces creep and fatigue despite the higher temperature reached at the tube crown.
3. The most critical tube section is located at the end of the last panel, where the temperature is maximum although the thermal stress is not as high as in the first panel.
4. The receiver efficiency diminishes when the tube diameter rises as the receiver area and, therefore, the thermal losses are higher.
5. The overall efficiency of the solar power plant is higher for smaller tube diameter since despite the fact that the solar field optical efficiency slightly increases with tube diameter as the solar field is larger, the decrease of the receiver efficiency is more acute.
6. The total cost of both heliostat field and receiver is lower for small diameter tubes because although the number of tubes and, therefore, the manufacturing costs of receiver increases when the tube diameter diminishes, the material costs of tubes, headers and heliostats are lower and dominate over the receiver manufacturing costs.
7. For a design ensuring 25 year receiver lifetime the minimum sCO_2 solar receiver cost, 345 €/kW_{th}, was obtained for the smallest pipe diameter.

CRediT authorship contribution statement

M. Fernández-Torrijos: Conceptualization, Methodology, Validation, Software, Writing – original draft, Writing – review & editing. **P.A. González-Gómez:** Conceptualization, Methodology, Validation, Software, Writing – original draft. **C. Sobrino:** Supervision, Conceptualization, Methodology, Writing – original draft, Writing – review & editing. **D. Santana:** Conceptualization, Supervision, Project administration, Funding acquisition.

Declaration of competing interest

The authors declare that they have no known competing financial interests or personal relationships that could have appeared to influence the work reported in this paper.

Acknowledgments

This research is partially funded by the Spanish government under the projects RTI2018-096664-B-C21 (MICINN/FEDER, UE) and RED2018-102431-T (AEI, MICINN) and the fellowship "Programa de apoyo a la realización de proyectos interdisciplinares de I + D para jóvenes investigadores de la Universidad Carlos III de Madrid 2019–2020" under the project ZEROGASPAIN-CM-UC3M (2020/00033/001), funded on the frame of "Convenio Plurianual Comunidad de Madrid-Universidad Carlos III de Madrid 2019–202".

Notation

Acronyms

AC	Auxiliary Compressor
CSP	Concentrating Solar Plants
HF	Heliostat Field
HX	Heat Exchanger
HTF	Heat Transfer Fluid
HTR	High Temperature Recuperator
LTR	Low Temperature Recuperator
MC	Main Compressor
PC	Pre-cooler
PB	Power Block
R	Receiver
SPT	Solar Power Tower
T	Turbine

Latin letters

A	Stress relaxation constant [−]
A_s	Cross-sectional area of a receiver tube [m^2]
B	Stress relaxation constant [−]
Bi	Biot number [−], $Bi = h_i\, t_t/k_w$
b	Characteristic Burgers vector [mm]
C	Cost [M€]
c_p	Specific heat [J/(kg K)]
D_c	Damage produced by creep [−]
D_f	Damage produced by fatigue [−]
D_L	Damage limit [−]
d_c	Damage produced by creep in one day [−]
d_f	Damage produced by fatigue in one day [−]
E	Modulus of elasticity [GPa]
F	View factor [−]
F_s	Safety factor [−]
f_r	Friction factor for smooth tubes [−]
$\bar{G}\,r$	Grashof number [−], $\bar{G}\,r = \frac{\rho_f\,(\rho_f - \bar{\rho})g\,(2\,r_i)^3}{\mu_f^2}$
H_t	Tube length [m]
h	Specific enthalpy [J/(kg K)]
h_i	sCO_2-to-wall convective heat transfer coefficient [W/(m^2 K)]
$\bar{h}_{nc}$	Natural convective heat transfer coefficient [W/(m^2 K)]
K	Strain hardening parameter [MPa]
K_{con}	Contraction coefficient [−]
K_{exp}	Expansion coefficient [−]
K_{safe}	Safety factor for creep damage calculation [−]

k_B	Boltzmann constant, 1.38064 × 10^{-23} [J/K]
k	Thermal conductivity [W/(m K)]
$\dot{m}$	sCO_2 mass flow rate [kg/s]
L_h	Total length of the header [m]
N_a	Number of allowable cycles [−]
N_c	Number of clips [−]
N_n	Number of header's nozzles [−]
N_p	Number of panels [−]
N_t	Number of tubes per panel [−]
N_s	Number of circumferential sections [−]
n	Strain hardening exponent [−]
Re	Reynolds number, $\mathrm{Re} = \frac{\rho_f u 2 r_i}{\mu_f}$ [−]
Pr	Prandtl number, $Pr = \frac{\mu_f c_{p,f}}{k_f}$ [−]
P	Pressure [MPa]
p	Order of accuracy [−]
$\dot{Q}$	Thermal power [W]
$\dot{Q}_{th,sf}$	Thermal power transferred from the solar field to the receiver HTF [W]
$\dot{Q}_{th,pb}$	Thermal power added to the power cycle [W]
$q_{c,l}$	Convective heat losses [W/m^2]
q	Radiative heat losses [W/m^2]
r	Radius [mm]
r_m	Grid refinement factor [−]
S	Maximum allowable stress value [MPa]
S_y	Yield strength [MPa]
$S_{y,c}$	Yield strength at cold temperature of the cycle [MPa]
T	Temperature [°C]
t	Thickness [mm]
t_R	Time to rupture [h]
t_{stab}	Stress relaxation stabilization time [h]
U	overall heat transfer coefficient [W/(m^2 K)]
u	sCO_2 velocity [m/s]
$\dot{W}$	Mechanical power [W]
z	Axial location [m]

Greek symbols

α	Ratio of cold to hot mass flow rate streams at LTR [−]
α_s	Surface absortivity [−]
β	Isobaric thermal expansion coefficient [1/K], $\beta = -\frac{1}{\rho_f}\frac{\partial \rho_f}{\partial T_f}$
η	Efficiency [−]
ϵ	Emissivity [−]
ε	Strain [mm/mm]
$\dot{\varepsilon}_c$	Shear stress modulus Creep strain rate [1/h]
μ	Shear stress modulus [MPa]
μ_f	Dynamic viscosity [Pa•s]
ν	Poisson's ratio [−]
ρ	Density [kg/m^3]
σ	Stress [MPa]
σ_{eff}	Creep effective stress [MPa]
σ_{LB}	Lower bound stress relaxation [MPa]
σ_s	Stefan-Boltzmann constant, 5.67 × 10^{-8} [W/(m^2 K^4)]
θ	Circumferential location [−]

Superscripts

E	Elastic
P	Plastic
relax	Relaxation

Subscripts

0	Reference conditions
amb	Ambient
c	Clips
co, a	Coating application
co, m	Coating material
eq	equivalent
f	sCO_2 stream
gr	Ground
h	Header
i	Inner
in	Inlet
n	Nozzles pulled from headers
o	Outer
out	Outlet
P	Pressure
sky	Sky
T	Thermal
t	Tube
w	Tube wall
we	Tube-to-header welds

References

[1] L. F. Cabeza, E. Galindo, C. Prieto, C. Barrenech, and A. I. Fernández. Key performance indicator in thermal energy storage: survey and assessment. Renew. Energy, 83:820–827.

[2] C. Murphy, Y. Sun, W. Cole, G. Maclaurin, C. Turchi, M. Mehos, The Potential Role of Concentrating Solar Power within the Context of DOEs 2030 Solar Cost Targets, Technical Report NREL/TP-6A20-71912, NREL, 2019.

[3] European Commission, Initiative for Global Leadership in Concentrated Solar Power. Implementation Plan. Integrated SET-Plan, Technical Report, SETIS, 2017.

[4] Y. Zhao, P. Li, H. Jin, Heat transfer performance comparisons of supercritical carbon dioxide and NaCl-KCl-$ZnCl_2$ eutectic salts for solar s-CO_2 Brayton cycle, Energy Procedia 142 (2017) 680–687.

[5] Y.C. Soo Too, M.D. López, H. Cassard, G. Duffy, R. Benito, R. Navio, Thermal performance and operation of a solar tubular receiver with CO_2 as the heat, J. Sol. Energy Eng. 139 (2017) 1–9, 0411004.

[6] ASME American Society of Mechanical Engineers, Boiler and Pressure Vessel Code, Code Case N-47: Nuclear Components, 1980.

[7] ASME American Society of Mechanical Engineers, Boiler and Pressure Vessel Code, Section III-NH, 2015.

[8] T.V. Narayanan, M.S.M. Rao, G. Carli, Structural design and life assessment of a molten salt solar receiver, J. Sol. Energy Eng. 107 (1985) 258–263.

[9] K. Nithyanandam, R. Pitchumani, Thermal and structural investigation of tubular supercritical carbon dioxide power tower receivers, Sol. Energy 135 (2016) 374–385.

[10] J. Ortega, S. Khivsara, J. Christian, C. Ho, J. Yellowhair, P. Dutta, Coupled modeling of a directly heated tubular solar receiver for supercritical carbon dioxide Brayton cycle: optical and thermal-fluid evaluation, Appl. Therm. Eng. 109 (2016) 970–978.

[11] T.W. Neises, M.J. Wagner, A.K. Gray, Structural design considerations for tubular power tower receivers operating at 650 °C, in: 8th International Conference on Energy Sustainability, 2014.

[12] P.A. González-Gómez, M.R. Rodríguez-Sánchez, M. Laporte-Azcué, D. Santana, Calculating molten-salt central-receiver lifetime under creep-fatigue damage, Sol. Energy 213 (2021) 180–197.

[13] F. Madani Sani, S. Huizinga, K.A. Esaklul, S. Nesic, Review of the API RP 14E erosional velocity equation: origin, applications,misuses, limitations and alternatives, Wear 426–427 (620–636) (2019).

[14] ASME American Society of Mechanical Engineers, Boiler and Pressure Vessel Code, Section VIII, Division 1, 2010.

[15] ASME American Society of Mechanical Engineers, Boiler and Pressure Vessel Code, Code Cases, 2015.

[16] M. Laporte-Azcué, P.A. González-Gómez, M.R. Rodríguez-Sánchez, D. Santana, Deflection and stresses in solar central receivers, Sol. Energy 195 (2020) 355–368.

[17] M. Wagner, T. Wendelin, SolarPILOT: a power tower solar field layout and characterization tool, Sol. Energy 171 (2018) 185–196.

[18] M.R. Rodrígez-Sánchez, C. Marugán-Cruz, A. Acosta-Iborra, D. Santana, Thermo-mechanical modelling of solar central receivers: effect of incident solar flux resolution, Sol. Energy 165 (2018) 43–54.

[19] C. Prieto, S. Fereres, F.J. Ruiz-Cabañas, A. Rodríguez-Sánchez, C. Montero, Carbonate molten salt solar thermal pilot facility: plant design, commissioning and operation up to 700 °c, Renew. Energy 151 (2020) 528–541.

[20] L. Yao, Z. Zou, A one-dimensional design methodology for supercritical carbon dioxide brayton cycles: integration of cycle conceptual design and components preliminary design, Appl. Energy 276 (2020) 115354.

[21] H.A. Muhammad, B. Lee, J. Cho, M. Imran, J. Cho, C. Roh, G. Lee, H. Shin, H. Sultan, Y.J. Baik, Investigating supercritical carbon dioxide power cycles

and the potential of improvement of turbine leakage characteristics via a barrier gas, Appl. Therm. Eng. 188 (2021) 116601.
[22] J.I. Linares, M.J. Montes, A. Cantizano, C. Sánchez, A novel supercritical CO_2 recompression Brayton power cycle for power tower concentrating solar plants, Appl. Energy 263 (2020) 114644.
[23] J.I. Linares, A. Cantizano, E. Arenas, B.Y. Moratilla, V. Martín-Palacios, L. Batet, Recuperated versus single-recuperator re-compressed supercritical co2 brayton power cycles for demo fusion reactor based on dual coolant lithium lead blanket, Energy 140 (2017) 307–317.
[24] B.S. Petukhov, Heat transfer and friction in turbulent pipe flow with variable physical properties, Adv. Heat Tran. 6 (1970) 503–564.
[25] C. Caliot, G. Flamant, Pressurized carbon dioxide as heat transfer fluid: influence of radiation on turbulent flow characteristics in pipe, AIMS Energy 2 (2) (2014) 172–182.
[26] A.J. Hacks, S. Schuster, D. Brillert, Stabilizing effects of supercritical CO_2 fluid properties on compressor operation, Int. J. Turbomach. Propuls. Power 4 (20) (2019) 1–11.
[27] L.F. González-Portillo, J.M. Muñoz-Antón, J.M. Martínez-Val, Supercritical carbon dioxide cycles with multi-heating in Concentrating Solar Power plants, Sol. Energy 207 (2020) 144–156.
[28] V.A. Kurganov, A.G. Kaptil'nyi, Velocity and enthalpy fields and eddy diffusivities in a heated supercritical fluid flow, Exp. Therm. Fluid Sci. 5 (4) (1992) 465–478.
[29] Y. Bae, H. Kim, Convective heat transfer to CO_2 at a supercritical pressure flowing vertically upward in tubes and an annular channel, Exp. Therm. Fluid Sci. 33 (2009) 329–339.
[30] E. Mohagheghian, A. Bahadori, L.A. James, Carbon dioxide compressibility factor determination using a robust intelligent method, J. Supercrit. Fluids 101 (2015) 140–149.
[31] D.L. Sibers, R.F. Moffatt, R.G. Schwind, Experimental, variable properties natural convection from a large,vertical, flat surface, J. Heat Tran. 107 (1985) 124–132.
[32] M. Modest, Radiative Heat Transfer, third ed., Academic Press, 2013.
[33] X. Berger, D. Buriot, F. Garnier, About the equivalent radiative temperature for clear skies, Sol. Energy 32 (1984) 725–733.
[34] I.E. Idelchik, Handbook of Hydraulic Resistance, Begell House, 1986.
[35] C.J. Roy, Review of code and solution verification procedures for computational simulation, J. Comput. Phys. 205 (2005) 131–156.
[36] P.J. Roache, Perspective: a method for uniform reporting of grid refinement studies, J. Fluid Eng. 116 (1994) 405–413.
[37] M.D. McMurtrey, L.J. Carroll, M. Messner, Creep-fatigue Behavior and Damage Accumulation of a Candidate Structural Material for Concentrating Solar Power Solar Thermal Receiver. Technical Report, Idaho National Laboratory, 2018.
[38] U.F. Kocks, Realistic constitutive relations for metal plasticity, Mater. Sci. Eng., A 317 (1–2) (2001) 181–187.
[39] H. Mecking, B. Nicklas, N. Zarubova, U.F. Kocks, A universal temperature scale for plastic flow, Acta Metall. 34 (3) (1986) 527–535.
[40] SpecialMetals, Inconel Alloy 740H, 2020. https://www.specialmetals.com/assets/smc/documents/alloys/inconel/inconel-alloy-740-h.pdf.
[41] R.L. Huddleston, An improved multiaxial creep-rupture strength criterion, J. Pressure Vessel Technol. 107 (4) (1985) 421–429.
[42] D.K. Fork, J. Fitch, S. Ziaei, R.I. Jetter, Life estimation of pressurized-air solar-thermal receiver tubes, J. Sol. Energy Eng. 134 (4) (2012), 041016.
[43] J. Bree, Elastic-plastic behaviour of thin tubes subjected to internal pressure and intermittent high-heat fluxes with application to fast-nuclear-reactor fuel elements, J. Strain Anal. Eng. Des. 2 (3) (1967) 226–238.
[44] W.R. Logie, J.D. Pye, J. Coventry, Structural integrity of chloride salt and sodium cooled advanced solar central alloy, in: SolarPaces Conference, 2020.
[45] P.A. González-Gómez, J. Gómez-Hernández, J.V. Briongos, D. Santana, Lifetime analysis of the steam generator of a solar tower plant, Appl. Therm. Eng. 159 (2019) 113805.
[46] M.D. McMurtrey, L.J. Carroll, M. Messner, Continuation Report: Creep-Fatigue Behavior and Damage Accumulation of a Candidate Structural Material for Concentrating Solar Power Solar Thermal Receiver, Technical Report, Idaho National Laboratory, 2018.
[47] M.R. Rodríguez-Sánchez, A. Soria-Verdugo, J.A. Almendros-Ibáñez, A. Acosta-Iborra, D. Santana, Thermal design guidelines of solar power towers, Appl. Therm. Eng. 63 (2014) 428–438.
[48] Q. Zhang, X. Li, Z. Wang, J. Zhang, B. El-Hefni, L. Xu, Modeling and simulation of a molten salt cavity receiver with dymola, Energy 93 (2015) 1373–1384.
[49] Z. Liao, X. Li, C. Xu, C. Chang, Z. Wang, Allowable flux density on a solar central receiver, Renew. Energy 62 (2014) 747–753.
[50] C. Marugán-Cruz, O. Flores, D. Santana, M. García-Villalba, Heat transfer and thermal stresses in a circular tube with non-uniform heat flux, Int. J. Heat Mass Tran. 96 (2016) 256–266.
[51] K. Nicol, Status of Advanced Ultra-supercritical Pulverised Coal Technology, Technical Report, International Energy Agency (IEA), 2013.
[52] C. Singer, R. Buck, R. Pitz-Paal, H. Müller-Steinhagen, Assessment of solar power tower driven ultrasupercritical steam cycles applying tubular central receivers with varied heat transfer media, J. Sol. Energy Eng. 132 (2010), 041010.
[53] C.K. Ho, J.E. Pacheco, Levelized Cost of Coating (LCOC) for selective absorber materials, Sol. Energy 108 (2014) 315–321.
[54] B. Kelly, Advanced Thermal Storage for Central Receivers with Supercritical Coolants, Technical Report, Abengoa Solar, 2010.
[55] J. Coventry, J. Campbell, Y.P. Xue, C. Hall, J. Kim, J. Pye, G. Burgess, D. Lewis, G. Nathan, M. Arjomandi, W. Stein, M. Blanco, J. Barry, M. Doolan, W. Lipinski, A. Beath, Heliostat Cost Down Scoping Study Final Report. Technical Report, Australian Solar Thermal Research Initiative (ASTRI), 2016.